# Largely Improving the Robustness and Lifetime of Triboelectric Nanogenerators through Automatic Transition between Contact and Noncontact Working States

Shengming Li,[†,‡,#] Sihong Wang,[†,#] Yunlong Zi,[†] Zhen Wen,[†] Long Lin,[†] Gong Zhang,[‡] and Zhong Lin Wang*[,†,§]

[†]School of Materials Science and Engineering, Georgia Institute of Technology, Atlanta, Georgia 30332-0245, United States, [‡]Department of Mechanical Engineering, Tsinghua University, Beijing 100084, China, and [§]Beijing Institute of Nanoenergy and Nanosystems, Chinese Academy of Sciences, Beijing, China. [#]S. Li and S. Wang contributed equally.

ABSTRACT Although a triboelectric nanogenerator (TENG) has been developed to be an efficient approach to harvest mechanical energy, its robustness and lifetime are still to be improved through an effective and widely applicable way. Here, we show a rational designing methodology for achieving a significant improvement of the long-term stability of TENGs through automatic transition between contact and noncontact working states. This is realized by structurally creating two opposite forces in the moving part of the TENG, in which the pulling-away force is controlled by external mechanical motions. In this way, TENGs can work in the noncontact state with minimum surface wear and also transit into contact state intermittently to maintain high triboelectric charge density. A wind-driven disk-based TENG and a rotary barrel-based TENG that can realize automatic state transition under different wind speeds and rotation speeds, respectively, have been demonstrated as two examples, in which their robustness has been largely improved through this automatic transition. This methodology will further expand the practical application of TENGs for long-time usage and for harvesting mechanical energies with fluctuating intensities.
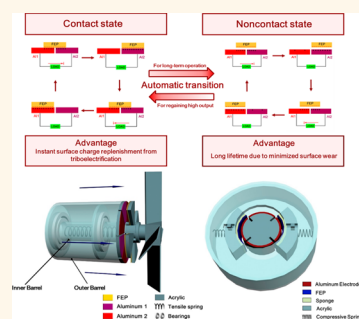
KEYWORDS: mechanical energy harvesting · triboelectric nanogenerators · automatic transition · contact and noncontact states · robustness improvement

In dealing with the increased energy consumption from limited traditional fossil fuel sources on the earth, studies on energy harvesting from the ambient environment have drawn extensive attention in recent decades.[1−6] Mechanical energy could be a promising solution if it can be harvested at a high efficiency and low cost. It not only can be utilized in a massive scale such as hydropower to potentially meet worldwide energy demands but also exists universally in human daily life and the natural environment so that it can be used effectively as independent and sustainable energy sources for small electronics and sensor networks.[7−12] Triboelectric nanogenerators (TENGs), which are based on the coupling between triboelectrification and electrostatic induction, have been proven to be effective for harvesting energy from mechanical agitations, with the features of high efficiency, low cost, and diversity in operation modes.[13−15]

Although researchers have established four basic modes—vertical contact mode, lateral sliding mode, single electrode mode, and freestanding mode—for TENGs and developed a variety of structures to harvest energy from many types of mechanical motions such as linear motion, vibration, and rotation,[16−23] the robustness and lifetime of TENGs for practical applications still have large room for improvement. Among the four basic modes of TENGs, the development of the freestanding mode serves as the initial step for solving this problem,
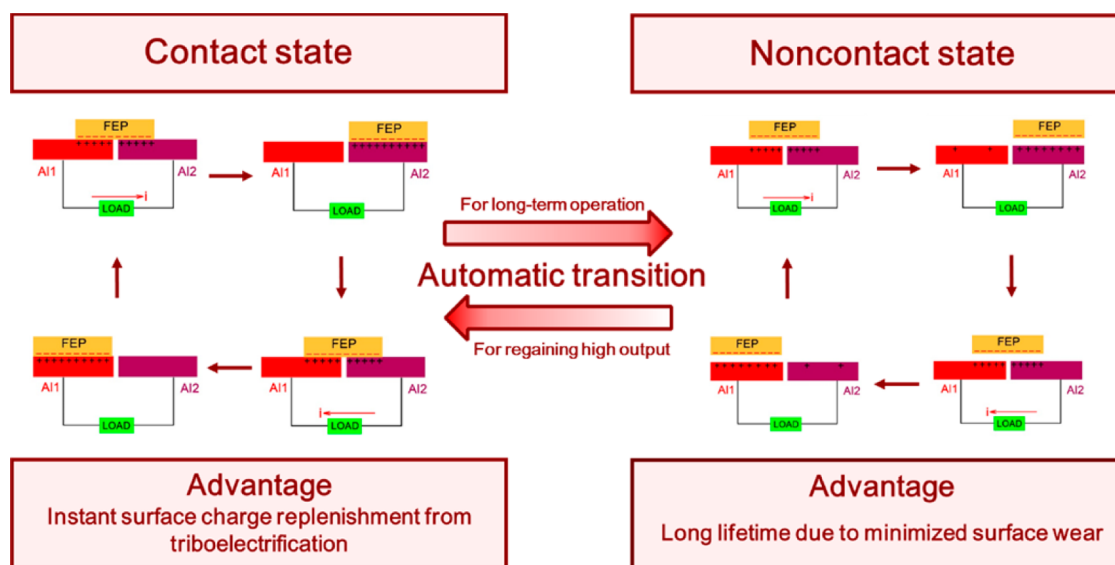
Figure 1. General working principles and advantages of the contact state, noncontact state, and the methodology of automatic transition between the two states for TENGs (taking a freestanding TENG for example).

which enables the generation of electricity in noncontact state with largely improved robustness, besides the traditional contact state. As shown on the left of Figure 1, when the freestanding TENG operates in the contact state, the sliding friction between the dielectrics (represented by fluorinated ethylene propylene (FEP) as an example) and the electrode surfaces generates static charges on both surfaces due to triboelectrification. At the same time, the alternative approach to the two electrodes by FEP drives electrons to flow back and forth between the two electrodes owing to electrostatic induction. Although the highest output performance can be obtained from this state due to the constant surface charge generation and the most effective electrostatic induction,[18,24−29] the surface wear from the contact sliding largely affects the long-term structural stability for TENGs. Both a cylindrical TENG[19] and a segmentally disk-based TENG[18] in contact state have been developed by our research group, while the long-term stability for these TENGs remains to be improved. On the other hand, since the triboelectric charges can remain in a dielectric for a period of time (especially for the electret materials), the TENG can work continuously in the noncontact state once the triboelectric charges have been generated (as shown on the right of Figure 1). Because the sliding motion of the FEP layer can still periodically reverse the induced electrical field distribution across the two electrodes, there is only a slight decrease in the output from the TENG as long as the vertical separation distance is much smaller than the lateral displacement of the two electrodes. In the noncontact state, the surface wear can be effectively minimized, which can dramatically enhance the stability and lifetime for TENGs (*e.g.,* the noncontact free-rotating disk TENG designed by our research group in 2014 that can work

only in noncontact state).[22,23,30] However, the gradual decay of the surface charges on the FEP will lead to the decrease of the electric output, which may limit the practical applications of the TENGs that keep working in the noncontact state.

In this paper, we have demonstrated a methodology to realize an automatic transition between the contact and noncontact states to achieve an unprecedented robustness with a good output performance in TENGs for practical applications. Through this, TENGs can work in the noncontact state for the majority of their working processes to minimize the surface wear, and they can also automatically transit into contact state intermittently for the replenishment of surface charges without interrupting the operation.[22,31−33] In this methodology, mechanical motions that are utilized to generate electricity for TENGs are also used to control the automatic state transition. The transition is realized by creating two opposite forces in the moving part of the TENG: one force to pull the moving part away from its counter stationary part, and the other force to push the parts together. The pulling force needs to have a positive relationship with the motion speed of the moving part, so that the two triboelectric surfaces will be pushed into contact at lower motion speed, but get separated by the pulling force at higher motion speed. In order to demonstrate the feasibility of this methodology, two specific TENG structures have been demonstrated as examples: (1) a disk-based TENG that uses the wind force to control the transition and (2) a rotary-barrel-based TENG that utilizes different spinning speeds of the barrel to realize the transition.

RESULTS AND DISCUSSION

The first example for demonstrating this methodology is a freestanding disk-based TENG to harvest wind
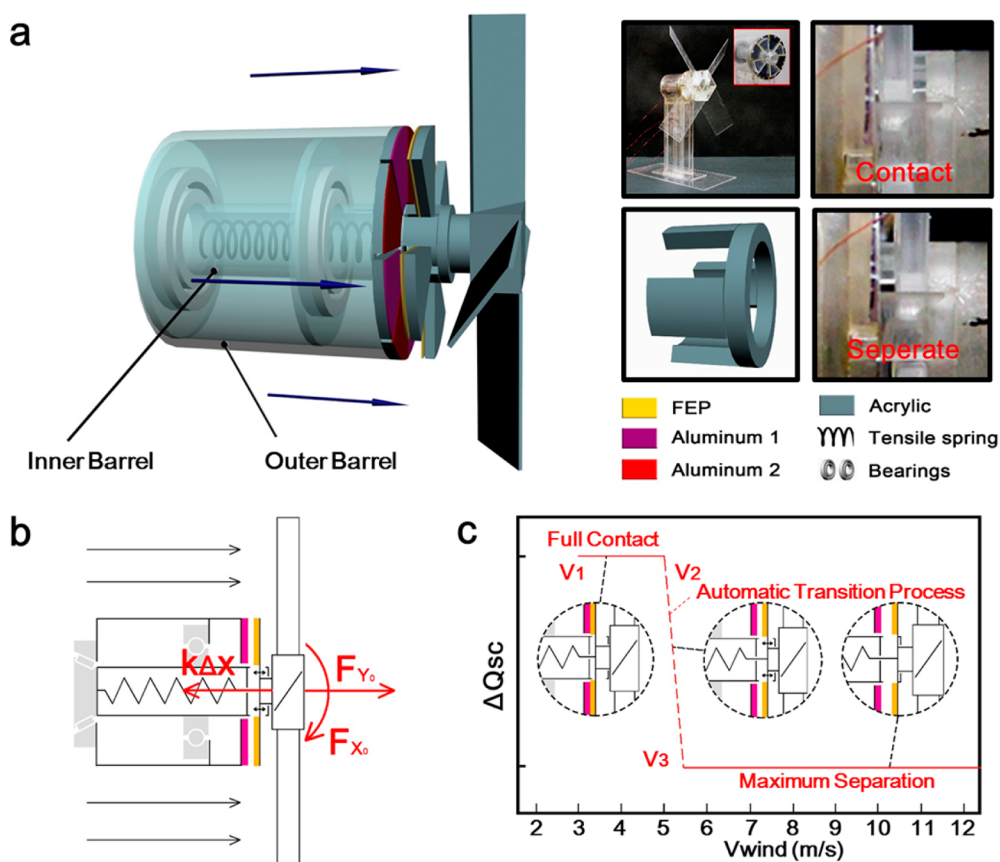
Figure 2. Device structure and working principles of the wind-driven TENG. (a) Schematic of the basic structure of the wind-driven TENG. The insets are the images of the whole structure as well as the disk TENG, the structure of the stopping ring, the amplified images of the TENG in contact state and noncontact state, as well as the figure legend. (b) Force diagram of the rotational part in the wind-driven TENG. (c) Theoretical relationship between short-circuit charge transfer and wind speed for the wind-driven TENG. The insets are the schematic diagram of full contact, automatic transition region, and maximum separation between the freestanding dielectric and the electrode.

energy (Figure 2). In the structural design of this TENG (Figure 2a), there are two major parts: the rotational inner acrylic barrel (~1 in. in diameter) that connects with the freestanding rotor of the disk TENG, and the stationary outer barrel (~3 in. in diameter) that connects with the stator of the TENG. Two bearings are used to link the two parts and enable the relative rotation. The entire framework is supported by a group of acrylic sheets. The rotor in the TENG is made of a uniformly distributed four-segmented acrylic sheet (~3 in. in diameter), with its surface laminated with a layer of FEP thin film (~50 μm in thickness) of the same shape. In order to further improve the charge density from the triboelectrification, the contacting surface of the FEP film is treated by inductive coupling plasma (ICP) to create nanostructures. The stator is made of an eight evenly segmented acrylic sheet (~3 in. in diameter, and the segments have the same shape and size as the ones on the rotor), with each segment laminated with one piece of aluminum foil (~50 μm in thickness) on the surface, which are connected into two groups of electrode to be the stator in a freestanding disk TENG. The automatic transition between the two states is achieved by creating two opposite forces on the rotor disk. The force pulling it apart from the stator's surface comes from a fan with four rectangular blades (~6 × 2.5 × 0.0625 in. in size) that is attached to the rotor through a small cylinder. In order to create this axial force as well as a tangential force to drive the rotation, each blade is tilted by 35°. On the other hand, the force to push the rotor to the stator comes from one tensile spring with the original tensile deformation Δx_0 = 17 mm inside the inner barrel (~k = 25.375 N/m as the spring constant), which connects the bottom of the inner barrel with the rotor disk. An acrylic stopping ring surrounding the cylinder is utilized to restrict the maximum vertical separation distance (Δx_{max} = 3 mm) between the freestanding rotor and the stator (the inset in Figure 2a). There are four feet extending out from the stopping ring to connect the inner barrel. There are two functions of these feet: (1) to drive the inner barrel to spin together with the rotor disk because the spring cannot be twisted; (2) to create a restriction for the separation distance between the rotor and the stator in the noncontact state (the insets in Figure 2a show the amplified images of this part of the TENG in both contact state and maximum noncontact state).

Under uniform wind (with the speed v_{wind}) blowing from the barrel side, the force on the tilted rectangle blades will have two perpendicular components: one along the tangential direction (F_{X_0}) and one along the axial direction (F_{Y_0}). They can be expressed by the following two equations:

$$F_{X_0} = \frac{1}{2} n\rho_{air}v_{wind}^2 ab(\cos^2\theta\sin\theta - \sin^2\theta\cos\theta)^2 \quad (1)$$

$$F_{Y_0} = \frac{1}{2} n\rho_{air}v_{wind}^2 ab(\cos^3\theta + \sin^3\theta)^2 \quad (2)$$

where n, a, and b are the number, length, and width of the rectangle fan blades, ρ_{air} is the density of the surrounding air, and θ is the tilt angle ($\sim35°$) of each blade. The force analysis for the movable rotor disk with the fan in the wind-driven TENG is depicted in Figure 2b. The separation between freestanding FEP and the electrodes is determined by the equilibrium between the F_{Y_0} and the tensile force ($f(v_{wind})$) in the spring, which can be expressed as

$$F_{Y_0} = f(v_{wind}) = k(\Delta x_0 + \Delta x) \quad (3)$$

where Δx_0 is the original deformation of the spring for the contact state between the rotor and the stator in the beginning, and Δx is the extra tensile deformation caused by the vertical separation. According to the conditions of vertical separation between the two disk parts in this TENG, the wind speed can be divided into three regions, with the boundary wind speed expressed as v_1, v_2, and v_3. In the first region (region I, $v_1 < v_{wind} < v_2$), F_{X_0} is larger than the friction force caused by original tensile deformation of the spring (i.e., $F_{X_0} > \mu k\Delta x_0$, where μ is the coefficient of sliding friction between the FEP and the aluminum). At the same time, F_{Y_0} is smaller than the tensile force from the original deformation of the spring (i.e., $F_{Y_0} < k\Delta x_0$). As a result, there is no vertical separation between the two disks, and the TENG is working in full contact state. In the second region (region II, $v_2 < v_{wind} < v_3$), F_{Y_0} exceeds the original tensile force from the spring, but is smaller than the tensile force under maximum separation distance (Δx_{max}) created by the stopping ring (i.e., $k\Delta x_0 < F_{Y_0} < k(\Delta x_0 + \Delta x_{max})$). As a result, the freestanding FEP disk is pushed to separate from the electrode disk, with the separation distance smaller than the maximum value ($0 < \Delta x < \Delta x_{max}$). This is the transition region between the contact working state (region I) and the noncontact working state with the maximum separation (region III). In the third region (region III, $v_{wind} > v_3$), F_{Y_0} is larger than tensile force under maximum separation ($F_{Y_0} > k(\Delta x_0 + \Delta x_{max})$), so that the separation reaches its maximum (~3 mm restricted by the stopping ring) and the TENG begins to work in the noncontact state with constant dielectric−electrode separation distance. The theoretical

relationship between short-circuit charge transfer and wind speed is illustrated in Figure 2c. In region I, the magnitude of the short-circuit charge transfer (ΔQ_{SC}) should equal the amount of triboelectric charges on the FEP. When the wind speed keeps increasing in region II, the vertical dielectric−electrode separation distance gradually gets larger, so that ΔQ_{SC} will gradually decrease. Then, in region III, because the separation distance stays constant at its maximum value, ΔQ_{SC} should remain unchanged in minimum under different wind speeds.

The experimental characterization of the automatic transition in this wind-driven TENG has been performed. Under a series of different wind speeds, 10 sets of short-circuit charge-transferred (ΔQ_{SC}), open-circuit voltage (V_{OC}), and short-circuit current (I_{SC}) were measured (Figure 3). As shown in Figure 3a, the relationship between ΔQ_{SC} and v_{wind} is similar to the theoretical curve predicted in Figure 2c. The measured $\Delta Q_{SC}-v_{wind}$ curve can be divided into three regions. In the first region with v_{wind} between v_1 (2.8 m/s) and v_2 (3.6 m/s), the ΔQ_{SC} remains at about a constant value of 34 nC due to the full contact between the rotor and the stator. In the second region, with v_{wind} between v_2 and v_3 (3.6−5.8 m/s), there is an evident decrease of ΔQ_{SC} from 34 nC to 27 nC with the increase of v_{wind}. This decrease is due to gradual separation of the two disks. Thus, it is the transition region. The profiles of the measured ΔQ_{SC} in this region are shown in Figure 3b. Subsequently, when the wind speed increases to v_3 (5.8 m/s), ΔQ_{SC} reaches another constant value of 27 nC, which is because the separation distance has reached the maximum value. This is the third region. From the full contact state to the noncontact state with maximum separation of the TENG, ΔQ_{SC} reduces by only $\sim21\%$, which demonstrates a good electric output. As for the open-circuit voltage (V_{OC}), it has the following relationship with the ΔQ_{SC}:[27,33]

$$V_{OC} = \frac{\Delta Q_{SC}}{C} \quad (4)$$

where C is the capacitance between the two groups of stationary electrodes, which remains constant during the operation. Therefore, V_{OC} should have a response to the wind speed similar to ΔQ_{SC}, which is shown by the measurement results in Figure 3c. Under v_{wind} from v_1 (2.8 m/s) to v_2 (4.1 m/s), there is the first constant value of V_{OC} (~88 V), representing the contact state of the TENG. The transition region from full contact to maximum separation appears with a v_{wind} of $v_2 \sim v_3$ (4.1−5.4 m/s), in which V_{OC} decreases from ~88 V to ~69 V. The profiles of the measured V_{OC} in this region are shown in Figure 3d. Finally there is the second constant V_{OC} of ~69 V when the freestanding rotor contacts the stopping ring, which happens when v_{wind} exceeds v_3 (5.4 m/s). It can be found that the decrease
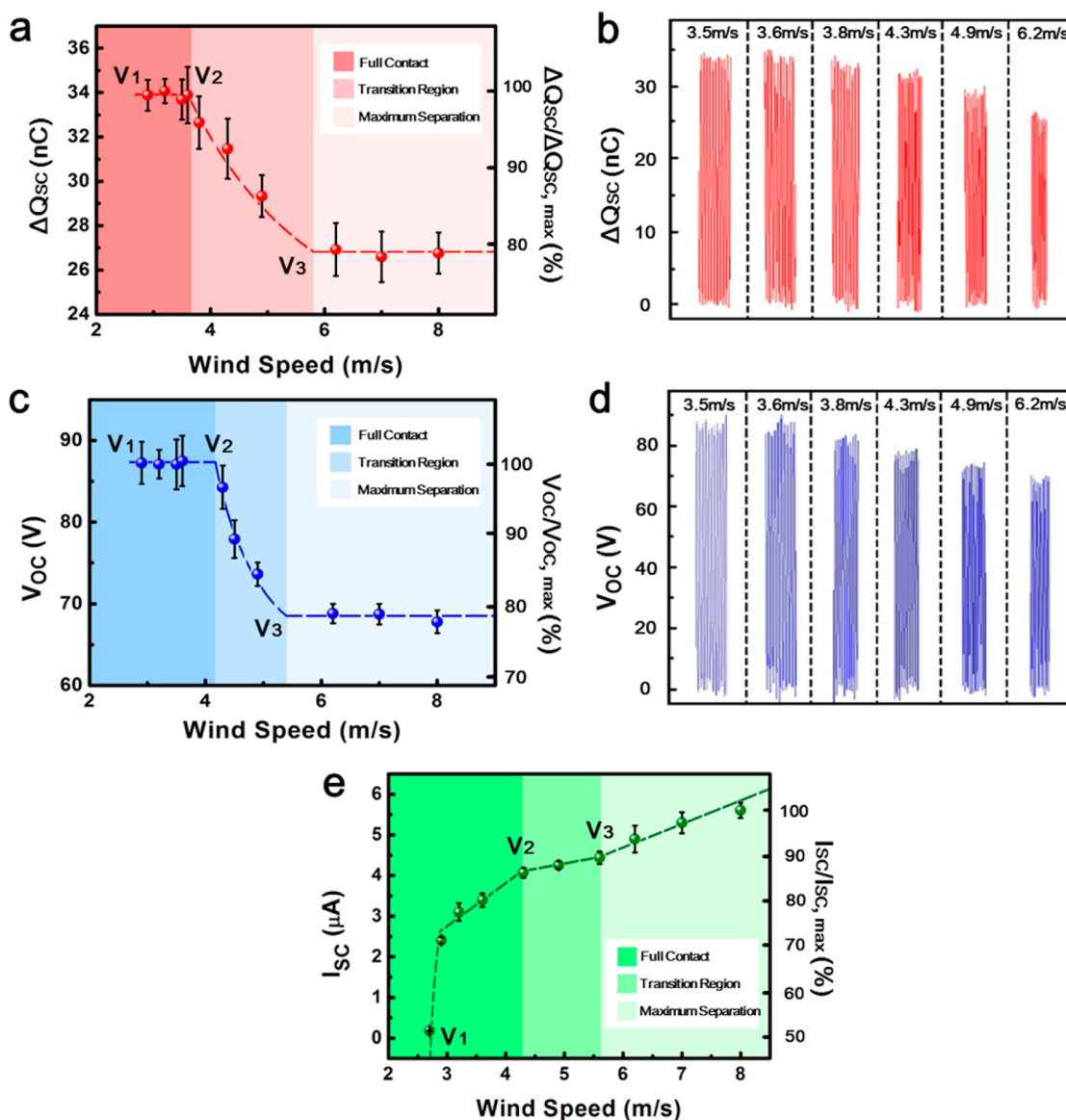
Figure 3. Electrical outputs of the wind-driven TENG under wind flows of different speed. (a, c, e) ΔQ_{SC}, V_{OC}, and I_{SC} of the TENG under different wind speeds, respectively. (b, d) Measured profiles of ΔQ_{SC} and V_{OC} in the state transition region.

of V_{OC} due to state transition is in the same degree as ΔQ_{SC}, and the boundary velocities (v_1, v_2, and v_3) for the three regions of the ΔQ_{SC} and the V_{OC} have a good correspondence. The relationship between I_{SC} and v_{wind} is shown in Figure 3e. Unlike the ΔQ_{SC} and the V_{OC}, the increase of v_{wind} leads to the monotonic increasing of I_{SC}. This is because I_{SC} has a proportional relationship with the charge transfer rate, *i.e.*, instantaneous rotation speed of the disk. In the transition region (*i.e.*, region II), although the increase of v_{wind} leads to a decrease of ΔQ_{SC}, the effect of increased charge transfer rate still dominates so that I_{SC} keeps the increasing trend. As a result, the higher wind speed could still generate a larger output power.

In order to demonstrate the supreme robustness and ultralong lifetime of the above wind-driven TENG due to the automatic transition between the noncontact

state and the contact state, long-term tests for both the wind-driven TENG and a TENG working purely in contact state as the comparison have been done (Figure 4). For the wind-driven TENG, wind blow was at a speed of 10.8 m/s to ensure a noncontact working state. In reality, natural wind always has a fluctuating speed, so that the entire TENG can get to the contact state occasionally for the triboelectric charges to get replenished from time to time. In order to simulate this behavior in the experiment, the blower to generate wind was stopped after every 10 000 rotation cycles for charge replenishment through triboelectrification at low wind speed. As shown in the SEM images of the FEP on the wind-driven TENG before and after 120 000 rotation cycles (Figure 4a,b), the nanostructures are preserved in good condition, showing minimized surface wear even after an extended operation period.
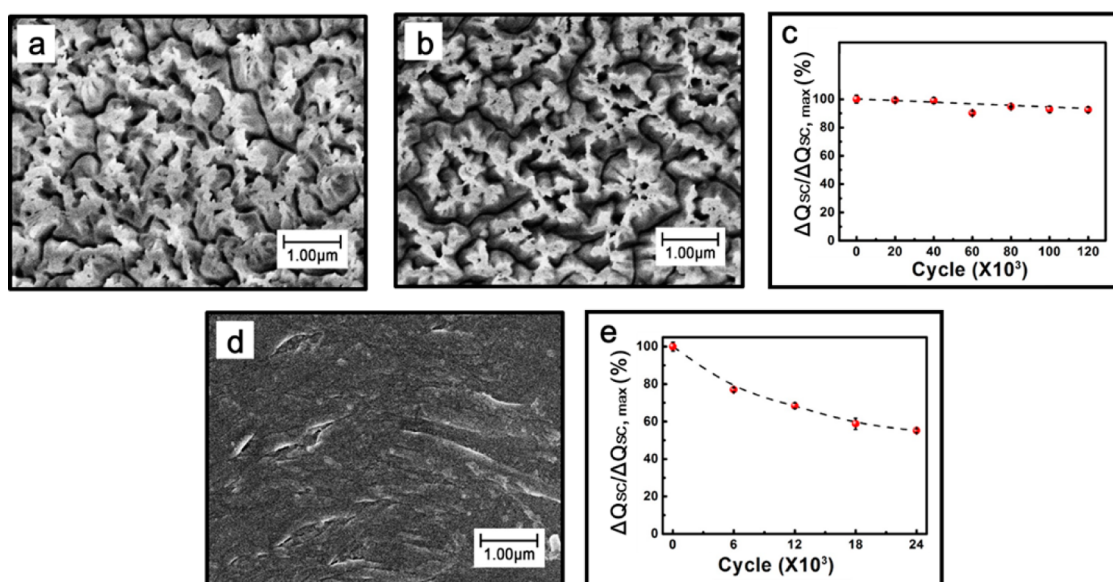
Figure 4. Stability tests for the wind-driven TENG and the contact-state TENG on the spinning motor system. (a, b) SEM images of the nanostructures on the FEP of the wind-driven TENG initially and after 120k rotating cycles (stopped for tribo-charge replenishment every 10k cycles) under a wind speed of 10.8 m/s. (c) Relationship between $\Delta Q_{SC}/\Delta Q_{SC,max}$ and the number of rotating cycles for the wind-driven TENG. (d) SEM image of the FEP after 2.4k rotations on the contact-state TENG. (e) Relationship between $\Delta Q_{SC}/\Delta Q_{SC,max}$ and the number of rotating cycles for the contact-state TENG.
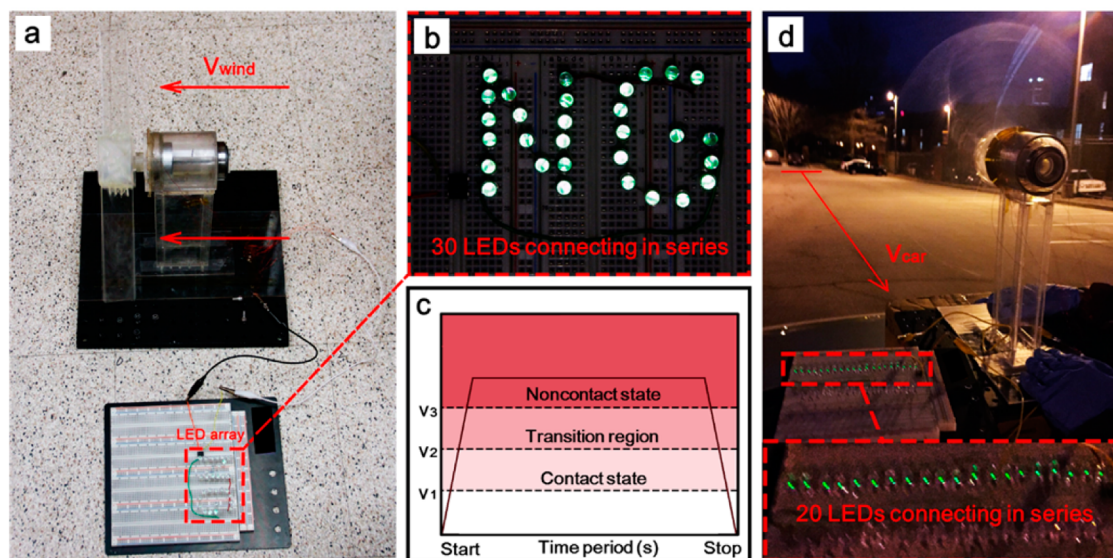

Figure 5. Applications of the wind-driven TENG to harvest energy from the ambient environment. (a, b) Images of the wind-driven TENG to light up 30 LEDs connected in series with wind at a speed of 10.8 m/s. (c) Simplified $v-t$ curve of a car (from start to stop). (d) Image of the wind-driven TENG to harvest wind energy generated by a moving car (v_{car} = 10 m/s) to light up 20 LEDs connected in series.

The long-term electric performance (represented by ΔQ_{SC}) of this wind-driven TENG is shown in Figure 4c. After 120 000 rotation cycles, nearly 95% of the maximum (original) ΔQ_{SC} is preserved in the wind-driven TENG. As a comparison, a disk-based TENG operating in the contact state was built, with the rotor disk and stator disk in the same shape and size as the wind-driven TENG. As shown in the SEM image, the nanostructures on the FEP have been almost completely wiped out due to constant wear after only 24 000 cycles (Figure 4d). Moreover, the ΔQ_{SC} is only 60% of the original value

(Figure 4e). Thus, the automatic transition between the contact state and the noncontact state brings a significant improvement in the TENG's robustness and lifetime.

Due to its outstanding long-term stability, the application of the wind-driven TENG can be largely expanded (Figure 5). As is demonstrated in Figure 5a and b, the electricity generated by this TENG in the noncontact state under a wind speed of 10.8 m/s is enough to light up 30 LEDs in series without surface wear. Moving objects (such as vehicles) are important resources for
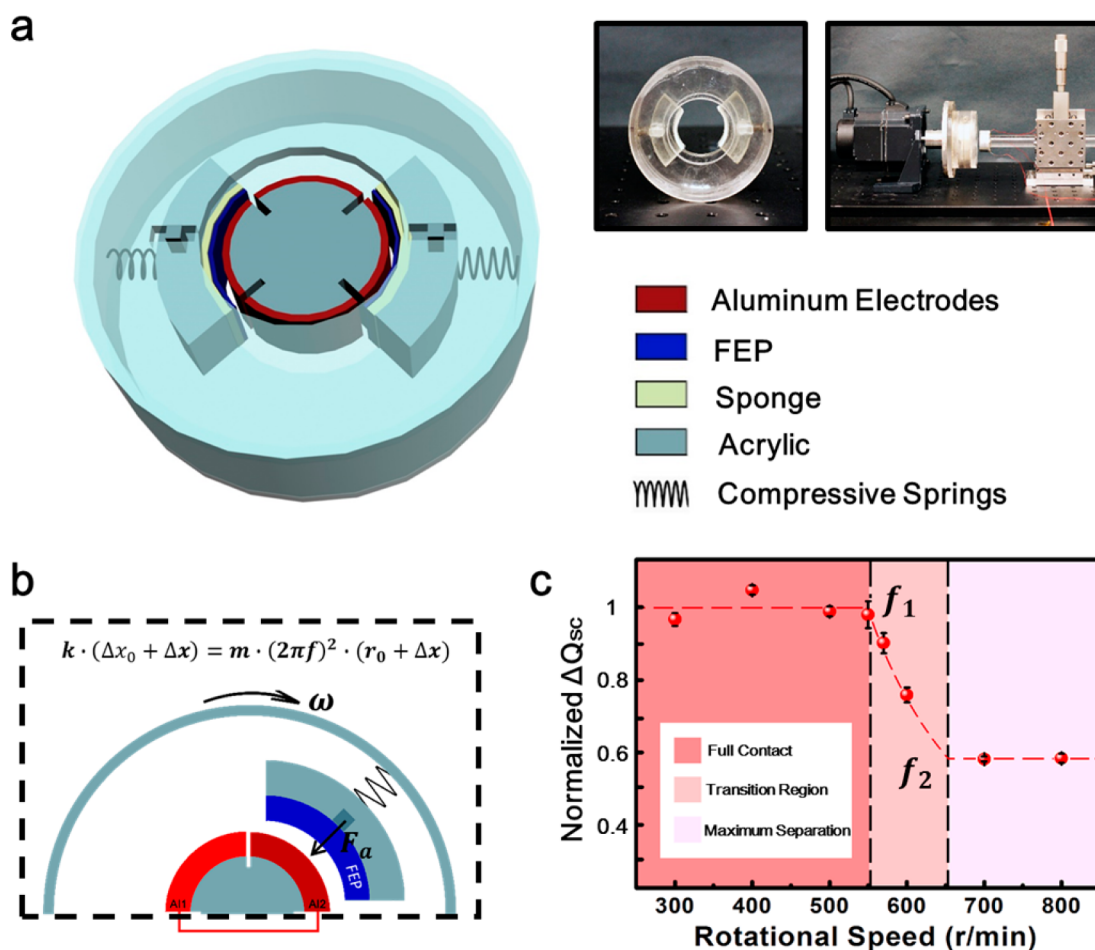
Figure 6. Device structure, mechanical working principle of the automatic transition, and electric output performance (ΔQ_{SC}) of the barrel-based TENG. (a) Schematic of the basic structure of the barrel-based TENG. The insets are an image of the freestanding barrel, an image of the entire spinning motor measurement system for the TENG, and the figure legend. (b) Mechanical working principle of the barrel-based TENG. (c) Relationship between normalized measured ΔQ_{SC} and the rotational speed of the freestanding barrel part.

generating wind with varied wind speed depending on the moving speed of the object. For example, the motion of a car can be simplified into three different stages (Figure 5c): acceleration, uniform motion, and deceleration. When the car is just started or nearly stopped, there will be charge replenishment from the contact state at low speed. While the car is running at high speed, the TENG will work in the noncontact state without surface wear. In this way, an automatic transition between the two states will be realized, which will largely increase the long-term stability of the wind-driven TENG. As shown in Figure 5d, 20 LEDs in series have been lighted by this TENG on a moving car at a speed of 10 m/s.

The second example for demonstrating the methodology of the automatic transition between contact state and noncontact state is a rotary-barrel TENG (Figure 6). This TENG is composed of a rotary acrylic barrel and a stationary acrylic cylinder (Figure 6a). Two segments are connected to the inner face of the barrel by two compressive springs, in opposite positions. Restricted by the trenches in the upper and bottom

surfaces of the TENG structure, these two segments can only have slight sliding along the radius direction to realize a vertical separation from the counter tribo-electric surface. Two rectangular FEP films (~50 μm in thickness, $\pi/4 \times 9/16$ in. in size) are laminated onto the inner face of the segments to form the freestanding rotary part of the TENG. Four aluminum foils (~50 μm in thickness, $\pi/4 \times 9/16$ in. in size) are attached onto the side face of the cylinder and then connected to two groups of electrodes as the stationary part of the TENG. During the electric measurement, the rotational barrel and the stationary cylinder were placed coaxially and driven by a spinning motor system (shown in the second inset in Figure 6a). In the stationary condition, the rotational freestanding FEP contacted firmly with one group of electrodes by the compressive force from an original compressive deformation Δx_0 ($\Delta x_0 = 0.25$ in.) of the springs.

In order to show the mechanism for realizing the automatic transition on this barrel TENG, the force analysis of one freestanding segment on the barrel TENG is carried out (Figure 6b). In this structure, the

centrifugal tendency of the rotational segment serves as the pull-away force, while the compressive force in the spring is the push force in the methodology. When the segment is rotating together with the barrel, there will be a balance between the centripetal force needed to maintain its circling motion and that provided by the spring (eq 5):

$$k(\Delta x_0 + \Delta x) = m(2\pi f)^2 (r_0 + \Delta x) \quad (0 \leq \Delta x \leq \Delta x_{max}) \quad (5)$$

where k ($\sim k = 50.76$ N/m), Δx, and Δx_{max} ($\sim \Delta x_{max} = 0.125$ in.) are the rate constant, the extra compressive deformation, and the maximum extra deformation of the spring, and m, f, and r_0 are the mass, the rotation speed, and radius of the segment ($\sim r_0 = 0.812$ in.), respectively. When the rotation speed f increases, the centripetal force that is demanded will be higher, which will lead to a larger deformation on the spring, thus a larger separation distance between the two triboelectric surfaces during the operation. Restricted by the length of the sliding tracks, the separation distance between the two surfaces has a maximum value. Thus, similar to the wind-driven TENG, the rotation speed for this barrel TENG can also be divided into three regions. Such behavior has been verified by the measured ΔQ_{SC} under a series of different rotation speeds, as shown in Figure 6c.

CONCLUSIONS

In summary, in order to fabricate robust and long-lifetime triboelectric nanogenerators while maintaining a high output performance, we demonstrated a new methodology to achieve the automatic transition between contact state and noncontact state in this paper, which helps not only to minimize surface wearing but also to maintain the saturated amount of tribo-charges. In the methodology, one pushing force and one pulling force are purposely created for the moving part of the TENG to control its relative position with the counter stationary part. The state transition is realized by automatically adjusting the pulling force through the change of applied mechanical agitations (that are also used to generate electricity). As a demonstrations of this methodology, two types of TENGs have been developed. The first one is a wind-driven disk-based TENG, in which the automatic state transition is realized through the different pull-away forces from different wind speeds. Because of the unique structural design, the TENG still generates a large output during the noncontact state. It has been clearly shown that such a transition results in a high stability and robustness of the TENG. The second demonstration is the rotary-barrel-based TENG, in which the automatic state transition was realized through the varied centrifugal tendency from different rotation speeds. Benefiting from this methodology, practical applications of TENGs can be largely expanded for long-time usage and for harvesting mechanical energies with fluctuating intensities, such as wind from the movement of vehicles.

EXPERIMENTAL SECTION

Fabrication of the Nanostructures on the Surface of the PFE Film. First, a piece of FEP film (~ 50 μm in thickness) was rinsed with ethanol, isopropyl alcohol, and deionized water, consecutively. Subsequently, 10 nm thick Au was sputtered on the surface of FEP, acting as the mask for the following etching process. Then we utilized ICP reactive ion etching to produce uniformly distributed nanostructures on the surface. In the ICP process, Ar, O_2, and CF_4 were used as the reaction gases with the ratio of 15.0, 10.0, and 30.0 sccm, respectively. A power source of 400 W was used to generate a large density of plasma, and another power source of 100 W was used to accelerate the plasma ions. Under such conditions, the FEP film was etched for 40 s.

Electric Measurement of the Wind-Driven TENG under Wind Flow of Different Speeds. A blower (~ 2700 cfm in airflow and 16 3/4 $\times$ 4 3/4 in. in outlet size) was used to generate wind. Wind speed was adjusted by changing the distance between the blower and the TENG. Before doing the electric measurement, we used the wind meter to measure the wind speed at the center of the fan. This value is used as the speed of the air flow for the TENG. The short-circuit charge transfer, open-circuit voltage, and short-circuit current were measured by a Keithley 6514 System (Stanford Research System).

Electrical Measurement of the Rotational Disk-Based TENG in Contact State. The rotational freestanding FEP with an acrylic disk was secured on a spinning motor (BX460AM-A, Oriental Motor), and the stationary disk with aluminum electrodes was attached onto a stationary XYZ linear translation stage (462-XYZ-M, Newport Incorporation). For both disks, the centers were aligned with the spinning axis. By adjusting the XYZ translation stage, the freestanding FEP was in contact with the electrodes. For a firm contact between the spinning motor and the freestanding FEP there was a buffer layer made of sponge. For the measurement of short-circuit charge transfer, open-circuit voltage, and short-circuit current, we used the same electrometer as the wind-blowing TENG system.

Electrical Measurement of the Barrel-Based TENG. The rotational barrel was secured on a spinning motor (BX460AM-A, Oriental Motor). The stationary cylinder with electrodes on the side face was attached to one side of an acrylic rod and then bonded on an XYZ translation stage (462-XYZ-M, Newport Incorporation). The centers of the barrel part and the cylinder were aligned with the spinning axis. Also, the cylinder was inserted into the barrel structure in the beginning for an original contact of the freestanding FEPs with the electrodes. For the measurement of short-circuit charge transfer, we used the same electrometer as for the wind-blowing TENG system.

Conflict of Interest: The authors declare no competing financial interest.

REFERENCES AND NOTES

1. Wang, Z. L.; Song, J. H. Piezoelectric Nanogenerators Based on Zinc Oxide Nanowire Arrays. *Science* **2006**, *312*, 242–246.
2. Wang, Z. L.; Zhu, G.; Yang, Y.; Wang, S.; Pan, C. Progress in Nanogenerators for Portable Electronics. *Mater. Today* **2012**, *15*, 532–543.

3. Oregan, B.; Gratzel, M. A Low-Cost, High-Efficiency Solar Cell Based on Dye-Sensitized Colloidal TiO$_2$ Films. *Nature* **1991**, *353*, 737–740.

4. Huynh, W. U.; Dittmer, J. J.; Alivisatos, A. P. Hybrid Nanorod-Polymer Solar Cells. *Science* **2002**, *295*, 2425–2427.

5. Tian, B.; Zheng, X.; Kempa, T. J.; Fang, Y.; Yu, N.; Yu, G.; Huang, J.; Lieber, C. M. Coaxial Silicon Nanowires as Solar Cells and Nanoelectronic Power Sources. *Nature* **2007**, *449*, 885–889.

6. Dresselhaus, M. S.; Chen, G.; Tang, M. Y.; Yang, R. G.; Lee, H.; Wang, D. Z.; Ren, Z. F.; Fleurial, J. P.; Gogna, P. New Directions for Low-Dimensional Thermoelectric Materials. *Adv. Mater.* **2007**, *19*, 1043–1053.

7. Wang, S.; Lin, Z.; Niu, S.; Lin, L.; Xie, Y.; Pradel, K. C.; Wang, Z. L. Motion Charged Battery as Sustainable Flexible-Power-Unit. *ACS Nano* **2013**, *7*, 11263–11271.

8. Mitcheson, P. D.; Miao, P.; Stark, B. H.; Yeatman, E. M.; Holmes, A. S.; Green, T. C. MEMS Electrostatic Micropower Generator for Low Frequency Operation. *Sens. Actuators A* **2004**, *115*, 523–529.

9. Naruse, Y.; Matsubara, N.; Mabuchi, K.; Izumi, M.; Suzuki, S. Electrostatic Micro Power Generation from Low-Frequency Vibration Such as Human Motion. *J. Micromech. Microeng.* **2009**, *19*, 94002.

10. Mitcheson, P. D.; Yeatman, E. M.; Rao, G. K.; Holmes, A. S.; Green, T. C. Energy Harvesting From Human and Machine Motion for Wireless Electronic Devices. *Proc. IEEE* **2008**, *96*, 1457–1486.

11. Chang, C.; Tran, V. H.; Wang, J.; Fuh, Y.; Lin, L. Direct-Write Piezoelectric Polymeric Nanogenerator with High Energy Conversion Efficiency. *Nano Lett.* **2010**, *10*, 726–731.

12. Latimer, A. M. Neutral Ecological Theory Reveals Isolation and Rapid Speciation in a Biodiversity Hot Spot. *Science* **2005**, *309*, 1722–1725.

13. Wang, Z. L. Triboelectric Nanogenerators as New Energy Technology and Self-Powered Sensors—Principles, Problems and Perspectives. *Faraday Discuss.* **2014**, *176*, 447–458.

14. Wang, S.; Lin, L.; Wang, Z. L. Triboelectric Nanogenerators as Self-Powered Active Sensors. *Nano Energy* **2015**, *11*, 436–462.

15. Wang, Z. L. Triboelectric Nanogenerators as New Energy Technology for Self-Powered Systems and as Active Mechanical and Chemical Sensors. *ACS Nano* **2013**, *7*, 9533–9557.

16. Niu, S.; Liu, Y.; Wang, S.; Lin, L.; Zhou, Y. S.; Hu, Y.; Wang, Z. L. Theory of Sliding-Mode Triboelectric Nanogenerators. *Adv. Mater.* **2013**, *25*, 6184–6193.

17. Bai, P.; Zhu, G.; Lin, Z.; Jing, Q.; Chen, J.; Zhang, G.; Ma, J.; Wang, Z. L. Integrated Multilayered Triboelectric Nanogenerator for Harvesting Biomechanical Energy from Human Motions. *ACS Nano* **2013**, *7*, 3713–3719.

18. Lin, L.; Wang, S.; Xie, Y.; Jing, Q.; Niu, S.; Hu, Y.; Wang, Z. L. Segmentally Structured Disk Triboelectric Nanogenerator for Harvesting Rotational Mechanical Energy. *Nano Lett.* **2013**, *13*, 2916–2923.

19. Bai, P.; Zhu, G.; Liu, Y.; Chen, J.; Jing, Q.; Yang, W.; Ma, J.; Zhang, G.; Wang, Z. L. Cylindrical Rotating Triboelectric Nanogenerator. *ACS Nano* **2013**, *7*, 6361–6366.

20. Wang, S.; Lin, L.; Xie, Y.; Jing, Q.; Niu, S.; Wang, Z. L. Sliding-Triboelectric Nanogenerators Based on in-Plane Charge-Separation Mechanism. *Nano Lett.* **2013**, *13*, 2226–2233.

21. Zhou, Y. S.; Zhu, G.; Niu, S.; Liu, Y.; Bai, P.; Jing, Q.; Wang, Z. L. Nanometer Resolution Self-Powered Static and Dynamic Motion Sensor Based on Micro-Grated Triboelectrification. *Adv. Mater.* **2014**, *26*, 1719–1724.

22. Wang, S.; Xie, Y.; Niu, S.; Lin, L.; Wang, Z. L. Freestanding Triboelectric-Layer-Based Nanogenerators for Harvesting Energy from a Moving Object or Human Motion in Contact and Non-contact Modes. *Adv. Mater.* **2014**, *26*, 2818–2824.

23. Lin, L.; Wang, S.; Niu, S.; Liu, C.; Xie, Y.; Wang, Z. L. Noncontact Free-Rotating Disk Triboelectric Nanogenerator as a Sustainable Energy Harvester and Self-Powered Mechanical Sensor. *ACS Appl. Mater. Interfaces* **2014**, *6*, 3031–3038.

24. Tokeshi, T.; Hiratsuka, K.; Sasaki, A.; Uchiyama, S.; Kajdas, C. Triboelectrification in Sliding/Rolling Contacts Using Twin-Ring Tribometer. *Tribol. Trans.* **2009**, *52*, 759–767.

25. Zhou, Y. S.; Liu, Y.; Zhu, G.; Lin, Z.; Pan, C.; Jing, Q.; Wang, Z. L. In Situ Quantitative Study of Nanoscale Triboelectrification and Patterning. *Nano Lett.* **2013**, *13*, 2771–2776.

26. Zhu, G.; Lin, Z.; Jing, Q.; Bai, P.; Pan, C.; Yang, Y.; Zhou, Y.; Wang, Z. L. Toward Large-Scale Energy Harvesting by a Nanoparticle-Enhanced Triboelectric Nanogenerator. *Nano Lett.* **2013**, *13*, 847–853.

27. Niu, S.; Liu, Y.; Wang, S.; Lin, L.; Zhou, Y.; Hu, Y.; Wang, Z. L. Theory of Sliding-Mode Triboelectric Nanogenerators. *Adv. Mater.* **2013**, *25*, 6184–6193.

28. Harper, W. R. Interpretation of Experiments on Frictional Electrification. *Nature* **1951**, *167*, 400–401.

29. Sessler, G. M.; Hillenbrand, J. Electromechanical Response of Cellular Electret Films. *Appl. Phys. Lett.* **1999**, *75*, 3405–3407.

30. Xie, Y.; Wang, S.; Niu, S.; Lin, L.; Jing, Q.; Yang, J.; Wu, Z.; Wang, Z. L. Grating-Structured Freestanding Triboelectric-Layer Nanogenerator for Harvesting Mechanical Energy at 85% Total Conversion Efficiency. *Adv. Mater.* **2014**, *26*, 6599–6607.

31. Lee, L. Dual Mechanism for Metal-Polymer Contact Electrification. *J. Electrost.* **1994**, *32*, 1–29.

32. Horn, R. G.; Smith, D. T.; Grabbe, A. Contact Electrification Induced by Monolayer Modification of a Surface and Relation to Acid–Base Interactions. *Nature* **1993**, *366*, 442–443.

33. Niu, S.; Wang, S.; Lin, L.; Liu, Y.; Zhou, Y. S.; Hu, Y.; Wang, Z. L. Theoretical Study of Contact-Mode Triboelectric Nanogenerators as an Effective Power Source. *Energy Environ. Sci.* **2013**, *6*, 3576–3583.